Electrically and magneto-dielectrically modified La^{3+} doped $Co_{0.3}Li_{0.1}Ca_{0.5}Fe_{2.1-x}La_xO_4$ spinel ferrites and their potential applications

Muhammad Imran Arshad[1,2,3**], Afeefa Dastgir[3], Faisal Alresheedi[4], Nasir Amin[3], Le Duc Tung[1,2], Mongi Amami[5], Nguyen Thi Kim Thanh[1,2*], Hira Zahid[3], Atta Ur Rehman[3***], Safa Ezzine[5], Jolly Jacob[6]

[1]*Biophysics Group, Department of Physics and Astronomy, University College London, Gower Street, London, WC1E 6BT, UK.*
[2]*UCL Healthcare Biomagnetic and Nanomaterials Laboratories, 21 Albemarle Street, London W1S 4BS, UK*
[3]*Department of Physics, Government College University, Faisalabad, 38000, Pakistan.*
[4]*Department of Physics, College of Sciences, Qassim University, Buraidah, 51452, Saudi Arabia.*
[5]*Department of Chemistry College of Sciences, King khalid university, P.O. Box 9004, Abha, Saudi Arabia.*
[6]*College of Arts and Sciences, Abu Dhabi University, UAE.*

Corresponding Author: : *ntk.thanh@ucl.ac.uk, **miarshadgcuf@gmail.com,

Muhammad.arshad@ucl.ac.uk, ***attaurrehman423@gmail.com

Abstract

Low temperature and more efficient sol-gel auto combustion process was utilized to synthesize $Co_{0.3}Li_{0.1}Ca_{0.5}Fe_{2.1-x}La_xO_4$ [**La-CLCF**] spinel ferrites (where $x = 0.00$, 0.01, 0.02, 0.03, 0.04, and 0.05). The La-CLCF sample's structural, optoelectrical, dielectric, and magnetic properties were examined as a result of La^{3+} doping. All synthesized La-CLCF samples have single-phased spinel matrix, according to X-ray diffraction (XRD) analysis. It was found that the crystallite size was 11.26 nm, and the bandgap energy of 3.45 eV for La^{3+} doping $x = 0.03$. The resistivity and activation energy both were increased with the substitution of La^{3+} in the CLCF spinel matrix, while the peak position of temperature coefficient of resistance (TCR) percentage was -3.92%/K at 372.56 K for sample $x = 0.03$. The alternating current conductivity improves with frequency, whereas the dielectric constant and tangent loss decrease as frequency increases. Further, the saturation magnetization and the microwave operating frequency for all the samples were reduced with the doping of La^{3+}. The minimum coercivity was 242.95 Oe at $x = 0.03$. Our study suggested that the $Co_{0.3}Li_{0.1}Ca_{0.5}Fe_{2.07}La_{0.03}O_4$ sample is tested as an active material for potential use in high-frequency applications, electromagnetic wave absorbing material, and evaluating the sensitivity of infrared (IR) detectors used in night vision bolometers.

Keywords: structural; resistivity; tangent loss; high-frequency; bolometers.

1

1 Introduction

Soft ferrites possess a low coercivity value, making them readily demagnetizable, and find widespread application in the electronics industry. They are utilized in various electronic components such as inductors, microwaves, and transformers, due to their high resistivity, permeability, temperature stability, cost-effectiveness, and minimal energy losses [1]. Moreover, the materials with higher temperature coefficient of resistance are useful for room-temperature infrared bolometers, and magnetic sensors [2-4]. Due to their low dielectric loss, excellent temperature performance, high resistivity, inexpensive, and high remanence ratio, lithium (Li^{1+}) and doped lithium (Li^{1+}) ferrites are interesting materials for microwave devices [5]. As laminating ferrite layers for multilayer chip inductors (MLCIs), Li^{1+} ferrites are also appropriate due to their excellent electromagnetic properties at higher frequencies, low sintering temperatures, and high Curie temperature [6]. Lithium ferrite exhibits a spinel-type crystal structure with the general formula AB_2O_4. Within this structure, metal cations (Li^{1+} and $Fe^{2+/3+}$) are distributed across both tetrahedral (A-) and octahedral (B-) sites. The arrangement of Li^{1+} and $Fe^{2+/3+}$ ions is a critical factor influencing the properties of lithium ferrite. In the crystal lattice, a deficiency of lithium can result in cation defects, the formation of secondary phases, and shortages of lithium, which is known for its relatively volatile nature [7].

Many researchers worked on the Li^{1+} and Li^{1+} substituted spinel ferrites (SFs) including Li-Co [8], Li-Ca [9], and Li-La [10] spinel ferrites. For lithium-ion batteries (LIBs) anode, the non-toxic and inexpensive $Li_{1.1}Co_{0.3}Fe_{2.1}O_4$ ferrite was demonstrated to be a superior electrochemical material in terms of rate capability, and specific capacity [8]. Randhawa *et al*., synthesized $Li_{0.25}Ca_{0.5}Fe_{2.25}O_4$ SFs using the solution combustion route and reported the crystallite size was 30 nm, whereas the lattice constant was 8.464 Å. At room temperature (*RT*), the tangent loss had small values, while the dielectric constant had high values suggesting it is useful for high-frequency devices [9]. Sattar *et al*., [10] reported $Li_{0.5}Fe_{2.5-x}La_xO_4$ (*x* = 0.0 and 0.1) SFs fabricated *via* the ceramic route. They observed that the substitution of rare earth La^{3+} ion does not affect the Li^{1+} ferrite's structural and magnetic behaviour. Therefore, the insertion of various dopant ions into the lithium ferrite lattice results in materials with novel and intriguing characteristics. The variations in these characteristics are caused by a cation distribution among the ferrite sublattice's tetrahedral (A-) and octahedral (B-) sites. This is due to the fact that the degree of inversion in doped Li^{1+} ferrites, and thus their parameters, are observed to be highly dependent on the pH value, preparation route, sintering temperature and time, amount and type of the dopant [11].

The precise characteristics of SFs, both in terms of their physical and chemical properties, are intricately dependent on the synthesis method employed, as well as a range of other factors including temperature, pH, and the choice of raw materials [12, 13]. The hydrothermal route [14], co-precipitation route [15-18], sol-gel combustion (SGAC) process [19-23], a solid-state method [24], and other synthetic procedures have been used by different researchers. Because of its benefits, such as low cost, the capability to control the grain size, simple method, and easy setup [25], we have preferred the SGAC method to prepare ferrites. In the current study, the impact of doping La^{3+} concentration on $Co_{0.3}Li_{0.1}Ca_{0.5}Fe_{2.1-x}La_xO_4$ [**La-CLCF**] where $x = 0.00, 0.01, 0.02, 0.03, 0.04$, and 0.05 SFs prepared using the SGAC process was examined. The main focus is to observe the impact of La^{3+} on structural, morphological, and optical bandgap energy, resistivity, dielectric, and magnetic behaviour of La-CLCF spinel ferrites.

2 Experimental parts

2.1 Materials used

The metal nitrates including $La(NO_3)_3.6H_2O$ (98.6%), $Ca(NO_3)_2.6H_2O$ (97.9%), $Co(NO_3)_2.6H_2O$ (97.9 %), $Fe(NO_3)_3.9H_2O$ (97%), $LiNO_3.6H_2O$ (99.99%), citric acid $(C_6H_8O_7)$, and ammonia solution were utilized as starting materials to synthesize La-CLCF samples powder.

2.2 Method of preparation

The SGAC process was used to prepare the sample powder. In this process, first, the metal nitrates solution and citric acid were prepared in a beaker with a molar ratio of 1:1, according to the stoichiometric calculation in deionized water. The breaker is put on magnetic stirring and adds ammonia solution to maintain the pH~7. After achieving the required solution pH, the temperature was maintained at 353 K of the magnetic stirrer, and continuous stirring. The solution first transforms into a gel and then the temperature of the magnetic stirrer is up to 553 K. The formed gel was transferred into ash with auto ignition and performed sintering at 1073 K for 8 h. The fluffy loose powder after sintering was grounded to change into well-fine powder. The SGAC preparation route for La-CLCF samples is illustrated in Fig. 1.

2.3 Characterization

To obtain a Bragg angle (2θ) in the range of $20^\circ – 60^\circ$, a D8 Bruker Advanced X-ray diffractometer having Cu-Kα radiation with a wavelength (λ) of 1.5418 Å was used. Scanning Electron Microscope (SEM), Nova Nano series 450 was utilized to record the micrographs of the La-CLCF material. UV-visible spectroscopy was performed to record the wavelength and

absorbance to measure the energy bandgap using Perkin Elmer, Model Lambda 25, UV-visible double spectrometer (UV-DS). KEITHLEY, Model 2401 source meter, IV Measurement Meter utilized two probes technique to measure the temperature-dependent resistivity. IM3536 series LCR meter was utilized for recorded dielectric parameters, and a vibrating sample magnetometer (VSM), Model VSM-175 was employed to measure the hysteresis loop.

3 Results and Discussion

3.1 Structural analysis

La-CLCF powder XRD spectra are depicted in Fig. 2 and the zoom part of the most intense (311) peak indicates a peak shift towards a greater angle with doping of La^{3+} in CLCF samples. It was observed that six peaks at different 2θ angles correspond to (220), (311), (222), (400), (422), and (511) planes of the spinel matrix [19, 26]. Fig. 3(a) indicates unit cell structure and Fig. 3(b) represents A- and B- sites in unit cell structure for the CLCF sample. Similarly, Fig. 3(c) indicates unit cell structure, and Fig. 3(d) represents A- and B- sites in unit cell structure for sample $x = 0.01$. The interplanar spacing (d), experimental lattice constant (a), and unit cell volume (V) were investigated [26] and these parameters were increased with the replacement of Fe^{3+} by La^{3+} in La-CLCF samples (as seen in Table 1). The peak shift and change lattice parameters may be due to the replacement of smaller radii Fe^{3+} (0.641 Å) with greater radii La^{3+} (1.154 Å) ions [27]. The crystallite size (D) was calculated [28, 29], and it was observed that it was 13.94 nm for $x = 0.0$ and decreased from 15.56 nm to 10.49 nm with the replacement of La^{3+} ions (as reported in Table 1). It may be due to La^{3+}–O^{2-} having greater bond energy than Fe^{3+}–O^{2-}, therefore high energy is required to add La^{3+} ions into B-site. This limits the crystal growth and crystallization, resulting in reduced crystallite sizes with the doping of La^{3+} [30]. The dislocation line density (δ) was determined and the "δ" was increased with decreasing "D" and *vice versa* [28]. The calculated values are given in Table 1 and it was observed that "δ" increases with the doping of the La^{3+} ion in the CLCF spinel matrix. The graphical picture of "D" and "δ" *versus* La^{3+} concentration (x) is depicted in Fig. 4(a). The A-site hopping length (L_A), B-site hopping length (L_B), and polaron radius (γ) were investigated [28], and the hopping length was linked with the lattice constant. Therefore, A- site hopping lengths, B- site hopping lengths, and polaron radius increase with the replacement of La^{3+} ions (as reported in Table 1). The L_A, L_B, and γ all enhance with the doping of La^{3+} in the CLCF lattice (as seen in Fig. 4(b)). The X-ray (d_X), bulk (d_B) and relative (d_R) densities were determined [28, 31], and listed in Table 1. The X-ray and relative densities reduce and bulk density increase with the replacement of dopant ions. The graphical representation of d_X, and

d_B densities with La^{3+} content (x) is depicted in Fig. 4(c). The porosity percentage (P%) of as-prepared La-CLCF samples was investigated [31], and the porosity percentage reduced from 41.44 % to 21.38 % for $x = 0.0$ to $x = 0.05$ and the graphical picture of P (%) *versus* La^{3+} doping (x) and relative density is depicted in Fig. 4(d). The decrease in the porosity percentage may be due to the increase of bulk density [32] and this can also arise through the substitution of Fe^{3+} ions with larger La^{3+} ions, resulting in reduced porosity [33].

3.2 Morphological analysis

SEM micrographs of La-CLCF power samples as depicted in Fig. 5(a-f). Because of the magnetic nature of SFs, all of the samples revealed a significant degree of agglomeration in irregular shape particle structure, and the particles are non-uniformly distributed. It can be seen from Fig. 5(a-f) that the agglomeration increases with the insertion of La^{3+} in the CLCF lattice. La^{3+} ions are larger compared to the host Fe^{3+} cations in the material. The size disparity can result in stronger electrostatic attraction particles. These attractive forces promote particle agglomeration as they tend to pull particles closer together [34].

3.3 Optical energy bandgap analysis

The bandgap energy (E_g) of La-CLCF samples was calculated using the Tauc-Plots formulism as depicted in Fig. 6(a-f). The Tauc relation is utilized to find the bandgap energy (E_g) [35];

$$\alpha h\upsilon = B(h\upsilon - Eg)^n \tag{1}$$

The incident photon energy, transition probability constant, and absorption coefficient are all represented by $h\upsilon$, A, and α respectively. Depending on whether the transition is direct or indirect, the constant 'n' equals 1/2 or 2. Fig. 5(a-f) shows the bandgap energies of La-CLCF samples. When the La^{3+} doping (x) increases from 0.0 to 0.05, the value of "E_g" increases from 2.73 to 3.82 eV. The incorporation of La^{3+} ions into the host lattice can cause changes in its crystal structure and lattice parameters. These structural modifications can affect the band structure, leading to an increase in the bandgap energy. The larger size of La^{3+} ions may introduce strain and alter the spacing between atoms, which in turn affects the electronic energy levels. The decrease in bandgap energy results in increasing crystallite size and vice versa [36]. Therefore, in our case with decreasing the crystallite size (as observed in XRD), the bandgap energy was increased.

3.4 Electrical analysis

Typically the resistivity (ρ) of SFs has ranged from $10^5\,\Omega$ cm to $10^9\,\Omega$ cm, and it can be influenced by some parameters, including the kind of dopant cation, the sintering

temperature, and the method of preparation. In this instance, the relation $\rho = RA/L$ is used to calculate the resistivity, where L and A indicate the thickness and cross-sectional area of the pellets, respectively, while R stands for the resistance. According to the Arrhenius relation, $\rho = \rho_o e^{\Delta E/k_B T}$, the resistivity decreases with increasing temperature, demonstrating the semiconductor nature of the SFs [37]. The resistivity (ρ) *versus* 1000/T (Arrhenius plots) of La-CLCF samples as seen in Fig. 7(a) are distributed into two linear regions. The first low-temperature region (Ferro region), and the resistivity are found to increase with increasing temperature. On the other hand, in the second high-temperature region (Para region), the resistivity decreases with increasing temperature. The exchange of electrons between the elements in more than one valence state and scattered unsystematically over lattice sites can be used to explain the conduction mechanism of ferrites [38]. Higher resistivity is the result of the La^{3+} ion replacements in the CLCF lattice. Every La^{3+} substitution may result in a reduction in the hopping between iron ions, such as $Fe^{2+} \rightarrow Fe^{3+}$ at *B*- sites, which helps to marginally enhance the resistivity. From Table 2, it was clear that the resistivity at RT (303 K) was reduced from 0.008×10^9 Ω cm to 14.275×10^9 Ω cm (graphically as seen in Fig.7(c)). Table 2 lists the Curie temperatures (T_C) for various compositions of the La-CLCF samples as obtained from Arrhenius plots (as seen in Fig. 7(a)). In Fig. 7(a), it is evident that "T_C" exhibits a trend to drop as La^{3+} content increases. The drift mobility (μ_d) was determined using the equation [39]:

$$\mu_d = \frac{1}{\eta e \rho} \qquad (2)$$

where $\eta = \frac{N_a d_B P_{Fe}}{M}$ is the concentration of electric charge carriers (M, P_{Fe} and N_a indicates molecular weight, number of Fe atoms, and Avogadro number) and $e = 4.8032451 \times 10^{-10}$ esu (charge of an electron). Higher resistivity SFs are found to have low drift mobility, and *vice versa*. The drift mobility versus temperature is depicted in Fig. 7(b). Fig. 7(b) shows that when the temperature rises, mobility rises as well. According to Table 2, a rise in La^{3+} contents causes a decrease in drift mobility (μ_d) of the charge carriers but not the electric carrier concentration (η). This shows that rather than a change in carrier concentration, the variation in resistivity with temperature in the mixed La-CLCF ferrite system is caused by a change in charge carrier drift mobility. The activation energy (ΔE) in SFs originates from the motion of the charge carrier. The hopping process and activation energy are closely related to one another, and the resistivity follows the same trend. The "ΔE" is also affected by the substitution of La^{3+} ions and determined using relation (3) which is given in Table 2.

$$\Delta E = 2.303 \times k_B \times 1000 \times slope \ (eV) \qquad (3)$$

The "ΔE" was increased from 0.307 eV to 0.786 eV as the La^{3+} doping increased from $x = 0.0$ to $x = 0.06$ (graphically as seen in Fig.7(c)). For evaluating the sensitivity of infrared detectors (IR) used in night vision bolometers, and magnetic sensors, the temperature coefficient of resistance (TCR) is extremely valuable [2-4, 40, 41]. The TCR data for pure and La-doped CLCF samples *versus* temperature were examined and illustrated in Fig. 8(a). The values of TCR% obtained from the peak position of Fig. 8(a) for La-CLCF samples are -3.54%/K at 413.23 K ($x = 0.0$), -4.04%/K at 402.90 K ($x = 0.01$), -2.77%/K at 393.22 K ($x = 0.02$), -3.92%/K at 372.56 K ($x = 0.03$), -4.21%/K at 363.66 K ($x = 0.04$), and -3.03%/K at 362.39 K ($x = 0.05$). Fig.8(b) shows La^{3+} concentration (x) *versus* TCR% at temperatures 303 K to 363 K (low-temperature range) and it was found the TCR% value maximum at $x = 0.01$. Fig.8(c) shows La^{3+} concentration (x) *versus* TCR% at temperatures 383 K to 523 K (medium temperature range) and it was found the TCR% value was maximum at $x = 0.03$. Finally, in Fig.8(d) La^{3+} contents (x) *versus* TCR% at temperatures 373 K to 623 K (high-temperature range) is shown, and the TCR% value was maximum at $x = 0.04$.

3.4 Dielectric analysis

The La-CLCF samples dielectric constant (ε'), dielectric tangent loss (*tan δ*), *ac* conductivity (σ_{ac}) and quality factor (Q factor) *versus* the log of frequency (log *f*) were measured. Fig. 9(a) showed the ε' *versus* the log *f* revealing a high ε' at low frequencies and a small value at high frequencies. The ε' decreases with frequency as a result of the electric dipoles' inability to align with the alternating electric field's rapid change. The Maxwell-Wagner model can explain interfacial polarization, a frequent occurrence in materials that are consistent with the well-known Koop's hypothesis [42, 43]. Charges that are restricted at grain boundaries enter the grains at high frequencies, lowering grain resistance and resulting in a low value of ε'. At low frequencies, the ε' of the samples was observed to be unexpectedly high.

Tangent loss (tan) is the term for the energy lost by the dielectric material when the dipoles are aligned to the electric field and lesser values of "tan δ" indicate more practical application [44]. The frequency response of tan δ for the La-CLCF samples is depicted in Fig. 9(b). The loss, which is particularly significant at around 10^2 kHz, reduced dramatically with rising frequency, eventually becoming frequency-independent at a higher frequency. In a dielectric material, the "tan δ" value governs the amount of energy dissipated. Koop's theory, which is based on polarization resonance with the applied field, can explain this behaviour. According to Koop's theory, grain boundaries have higher resistance at lower frequencies, therefore hopping electrons from one site to another requires more energy. As a result, at lower

frequencies, energy loss is high. In contrast, grain boundaries have lower resistivity at higher frequencies, requiring less energy for electrons to move between two ions at lattice sites [45].

The frequency response of the La-CLCF samples ac conductivity (σ_{ac}) is shown in Fig. 9(c). For all of the samples, the "σ_{ac}" was excessively low at lower frequencies and the hopping of charge carriers between Fe^{2+} and Fe^{3+} lattice sites were responsible for the increase in "σ_{ac}" at high frequencies. Maxwell–Wagner's and Koop's theories can also explain the variation in ac conductivity. According to these theories, the dielectric structure is composed of two layers: The grain boundaries between well-conducting ferrite grains are formed by a thin layer of poorly conducting material. At low frequencies, poor-conducting grain boundaries become more active, leading to small ac conductivity, whereas high-conductivity ferrite grains are effective at high frequencies, resulting in larger ac conductivity and decreased electron hopping frequency between the ions.

To estimate the efficiency of some electrical devices, the quality factor (Q-factor) examines the link between stored energy and the rate of energy dissipation. The Q-factor of ferrite materials is an important factor in the design of electrical devices. The variations in the Q-factor of La-CLCF samples with frequency are depicted in Fig. 9(d). It was clear from Fig. 9(d) that the Q-factor increased with the applied frequency.

Fig.10(a) showed that La^{3+} concentration (x) $versus$ dielectric constant at frequencies 15 Hz to 500 kHz (low-frequency range) and the dielectric constant was found to be maximum at $x = 0.04$. In Fig.10(b) of La^{3+} concentration (x) $versus$ dielectric constant at frequency 1 MHz to 8 MHz (high-frequency range), the dielectric constant was seen also as a maximum at $x = 0.04$. Fig.10(c) showed that La^{3+} doping (x) $versus$ "tan δ" at frequencies 15 Hz to 500 kHz (low-frequency range) and the "tan δ" minimum at $x = 0.0$, while, in Fig.10(d) of La^{3+} concentration (x) $versus$ tangent loss at frequency 1 MHz to 8 MHz (high-frequency range), the tangent loss was observed minimum at $x = 0.01$. In Fig.10(e) of La^{3+} concentration (x) $versus$ ac conductivity at frequency 15 Hz to 500 kHz (low-frequency range), the ac conductivity was minimum at $x = 0.03$, while Fig.10(f) of that La^{3+} concentration (x) $versus$ ac conductivity at frequency 1 MHz to 8 MHz (high-frequency range) revealed that the tangent loss was also minimum at $x = 0.01$.

3.5 Hysteresis loop analysis

Hysteresis loops (M–H loops) of La^{3+} substituted CLCF samples with a low coercive field, are shown in Fig. 11(a). Table 3 revealed the values of all the magnetic parameters. The La-CLCF sample's saturation magnetization (M_S) and remanent magnetization (M_r) were

maximum for $x = 0.01$, while remanent magnetization was minimum (21.78 emu/g) at $x = 0.03$ which may be due to nonmagnetic La^{3+} ions replacement in the CLCF spinel lattice. Moreover, the "D" was reduced with the replacement of La^{3+} ions in the CLCF sample (as seen in Table 1). The introduction of La^{3+} content, with $x = 0.01$, results in an increase in M_S to 117.33 emu/g. Following this point, there is a gradual decrease in M_S, dropping to 83.22 emu/g with increasing La^{3+} doping. The magnetic characteristics of the SFs are substantially influenced by factors such as cation distribution, particle size, and A-B interactions [46-49]. The notable increase in M_S for $x = 0.01$ can be attributed to the redistribution of cations within the A- and B- sites. When non- magnetic La^{3+} was substituted for Fe^{3+} ($5u_B$), which was the main contributor to the magnetic properties at B- site of the SFs, the result may be explained by the weak A-O-B super-exchange interaction. It is well known that the magnetic properties of SFs with the AB_2O_4 spinel crystal matrix depend on the cation content at the A- and B- sites. AB_2O_4 is characterized by exchange interactions (A-A) and (B-B), while superexchange interaction is represented by (A-B). In comparison to the (A-A) and (B-B) interactions, the (A-B) interaction exhibits significantly stronger interactions. Because of the occupancy of La^{3+} ions, the concentration of Fe^{3+} ions at the B- site of the SFs decreased, reducing the (B-B) interactions and, as a result, the (A-B) super-exchange interactions. In other words, the strongly magnetic Fe^{3+} ($5u_B$) ions are the main cause of the B- site magnetic behaviour in SFs. As non-magnetic La^{3+} ions gradually replaced magnetic Fe^{3+} ions, the B-B (Fe^{3+}-Fe^{3+}) interactions decreased. Thus, a decrease in the magnetic moment with higher La^{3+} doping can be attributed to a reduction in the net magnetic moment [50, 51]. For $x = 0.01$, the maximum coercivity (H_C) was found, and the minimum coercivity was 242.95 Oe for sample $x = 0.03$. The low coercivity indicates the soft nature of the materials and is useful for electromagnetic wave absorbing materials in C-band frequencies [52]. The coercivity depends on extrinsic factors such as grain size, surface effects, and the movement of the domain walls. Finally, the change in magnetic parameters may be due to the doping of the La^{3+} ion with the Fe^{3+} ion, which modifies the orientation of the Fe^{3+} ion's magnetic moment, and the arrangement of Fe^{3+} ions in the crystal structure is changed. The soft magnetic nature of La-CLCF SFs changed with La^{3+} doping and is good for high-frequency applications, including circulators, and inductor cores. With increasing La^{3+} content, the squareness ratio ($S_q = M_r/M_s$) was decreased as reported in Table 3 and it was observed that the minimum S_q was 0.247 for $x = 0.03$. The value of "S_q", less than 0.5 represents particle magneto static interaction [43]. Therefore, the S_q ratio for all La-CLCF samples showed the interaction of particles by magnetostatic interaction. The anisotropy

constant (K) was determined *via* the equation: $K = \frac{H_C \times M_S}{0.9}$ [53] and the value of "K" (as seen in Table 3) is affected by M_S and H_C. The microwave operating frequency was calculated using the formula: $\omega_m = 8\pi^2 M_s \gamma$ (where γ = 2.8 MHz/Oe is the gyromagnetic ratio) [54-57] and values of "ω_m" was found to be in the gigahertz range as seen in Table 3. According to Fig. 11(b), La-CLCF samples are a favorable choice for high-frequency devices because of their microwave frequency response.

4 Conclusions

In conclusion, the SGAC technique was used to successfully synthesize La-CLCF samples. Based on the XRD data, single-phase spinel-type ferrites were found in all the compositions. The energy bandgap plots showed a decreasing trend and had a value of 3.45 eV for sample x = 0.03. The resistivity was 1.523×10^9 Ω cm and the activation energy of 0.531 eV at x = 0.03, while the peak position of TCR was -3.92%/K at 372.56 K for x = 0.03. When frequency increased, both the loss tangent and the dielectric constant experienced a sharp decline. The M_S was reduced with the insertion of La^{3+} and had a value of 87.91 emu/g, while small coercivity was 242.95 Oe observed for the sample x = 0.03. Due to its easy to fabricate, low cost, low dielectric tangent loss, high resistivity, small coercivity, and high TCR%, the current research revealed that the sample x = 0.03 is effective for high-frequency applications, electromagnetic wave absorbing material, and evaluating the sensitivity of infrared detectors (IR) used in night vision bolometers.

References

[1] N. Dhanda, P. Thakur, A.C.A. Sun, A. Thakur, Structural, optical and magnetic properties along with antifungal activity of Ag-doped Ni-Co nanoferrites synthesized by eco-friendly route, Journal of Magnetism Magnetic Materials 572 (2023) 170598.

[2] H. Li, K. Chu, X. Pu, S. Zhang, G. Dong, Y. Liu, X. Liu, A-site mixed-valence co-doping to optimize room-temperature TCR of polycrystalline $La_{0.8}K_{0.04}Ca_{0.16-x}Sr_xMnO_3$ ceramics, Ceramics International 46(13) (2020) 20640-20651.

[3] X. Yu, H. Li, K. Chu, X. Pu, X. Gu, S. Jin, X. Guan, X. Liu, A comparative study on high TCR and MR of $La_{0.67}Ca_{0.33}MnO_3$ polycrystalline ceramics prepared by solid-state and sol-gel methods, Ceramics International 47(10) (2021) 13469-13479.

[4] Z. Yu, H. Li, Z. Li, X. Yu, S. Jin, X. Guan, H. Zhang, Q. Chen, X. Liu, Improved room-temperature TCR and MR of $La_{0.9-x}K_xCa_{0.1}MnO_3$ ceramics by A-sites vacancy and disorder degree adjustment, Journal of Materials Science: Materials in Electronics 32 (2021) 8848-8862.

[5] S. Watawe, B. Sarwade, S. Bellad, B. Sutar, B. Chaugule, Microstructure and magnetic properties of Li-Co ferrites, Materials Chemistry and Physics 65(2) (2000) 173-177.

[6] Z. Yue, J. Zhou, X. Wang, Z. Gui, L. Li, Preparation and magnetic properties of titanium-substituted LiZn ferrites via a sol-gel auto-combustion process, Journal of the European Ceramic Society 23(1) (2003) 189-193.

[7] R. Verma, P. Thakur, A.C.A. Sun, A. Thakur, Investigation of structural, microstructural and electrical characteristics of hydrothermally synthesized $Li_{0.5-0.5x}Co_xFe_{2.5-0.5x}O_4$, (0.0≤ x≤ 0.4) ferrite nanoparticles, Physica B: Condensed Matter 661 (2023) 414926.

[8] E.E. Ateia, M.A. Ateia, M.G. Fayed, S. El-Hout, S.G. Mohamed, M. Arman, Synthesis of nanocubic lithium cobalt ferrite toward high-performance lithium-ion battery, Applied Physics A 128(6) (2022) 1-10.

[9] B. Randhawa, J. Singh, Physico-chemical studies on synthesis, characterization, and magnetic properties of Li–Ca–Zn nanoferrites, Journal of nanoparticle research 15(1) (2013) 1-10.

[10] A. Sattar, A. Wafik, H. El-Sayed, Infrared Spectra and Magnetic Studies of Trivalent Doped Li-Ferrites, Physica Status Solidi 186(3) (2001) 415-422.

[11] G. Aravind, D. Ravinder, V. Nathanial, Structural and electrical properties of Li–Ni nanoferrites synthesised by citrate gel autocombustion method, Physics research international 2014 (2014).

[12] P. Punia, P. Thakur, R. Kumar, R. Syal, R. Dhar, A. Thakur, Synthesis and characterization of Ca substituted Ni-Zn nanoferrites-microstructural, magnetic and dielectric analysis, Journal of Alloys and Compounds 928 (2022) 167248.

[13] S. Taneja, P. Thakur, B. Ravelo, A. Thakur, Nanocrystalline samarium doped nickel-zinc-bismuth ferrites: investigation of structural, electrical and dielectric properties, Materials Research Bulletin 154 (2022) 111937.

[14] A.N. Alqarni, M. Almessiere, S. Güner, M. Sertkol, S.E. Shirsath, N. Tashkandi, A. Baykal, Structural and magnetic properties of hydrothermally synthesized Bi-substituted Ni–Co nanosized spinel ferrites, Ceramics International 48(4) (2022) 5450-5458.

[15] K. Hussain, N. Amin, M.I. Arshad, Evaluation of structural, optical, dielectric, electrical, and magnetic properties of Ce^{3+} doped $Cu_{0.5}Cd_{0.25}Co_{0.25}Fe_{2-x}O_4$ spinel nano-ferrites, Ceramics International 47(3) (2021) 3401-3410.

[16] N. Amin, M. Akhtar, M. Sabir, K. Mahmood, A. ALIa, G. Mustafa, M. Hasan, A. Bibi, M. Iqbal, F. Iqbal, Synthesis, structural and optical properties of zn-substituted Co W-ferrites by coprecipitation method, Journal of Ovonic Research 16(1) (2020) 11-19.

[17] I. ALIa, N. Amin, A. Rehman, M. Akhtar, M. Fatima, K. Mahmood, A. ALIa, G. Mustafa, M. Hasan, A. Bibi, Electrical and magnetic properties of $BaCo_xCd_{2-x}Fe_{16}O_{27}$ W-type hexaferrites (0≤ x≤ 0.5), Digest Journal of Nanomaterials and Biostructures 15(1) (2020), 67-73.

[18] A. Aslam, A.U. Rehman, N. Amin, M.A. un Nabi, Q. ul ain Abdullah, N. Morley, M.I. Arshad, H.T. Ali, M. Yusuf, Z. Latif, Lanthanum doped $Zn_{0.5}Co_{0.5}La_xFe_{2-x}O_4$ spinel ferrites synthesized via co-precipitation route to evaluate structural, vibrational, electrical, optical, dielectric, and thermoelectric properties, Journal of Physics and Chemistry of Solids 154 (2021) 110080.

[19] A.U. Rehman, N. Morley, N. Amin, M.I. Arshad, M.A. un Nabi, K. Mahmood, A. Ali, A. Aslam, A. Bibi, M.Z. Iqbal, Controllable synthesis of La^{3+} doped $Zn_{0.5}Co_{0.25}Cu_{0.25}Fe_{2-x}La_xO_4$ (x= 0.0, 0.0125, 0.025, 0.0375, 0.05) nano-ferrites by sol-gel auto-combustion route, Ceramics International 46(18) (2020) 29297-29308.

[20] S. Wadgane, S. Alone, A. Karim, G. Vats, S.E. Shirsath, R. Kadam, Magnetic field induced polarization and magnetoelectric effect in $Na_{0.5}Bi_{0.5}TiO_3$–$Co_{0.75}Zn_{0.25}Cr_{0.2}Fe_{1.8}O_4$ multiferroic composite, Journal of Magnetism and Magnetic Materials 471 (2019) 388-393.

[21] V. More, R. Borade, K. Desai, V. Barote, S. Kadam, V. Shinde, D. Kulkarni, R. Kadam, S. Alone, Site Occupancy, Surface Morphology and Mechanical Properties of Ce^{3+} Added Ni–Mn–Zn Ferrite Nanocrystals Synthesized Via Sol–Gel Route, Nano 16(05) (2021) 2150059.

[22] G. Hussain, I. Ahmed, A.U. Rehman, M.U. Subhani, N. Morley, M. Akhtar, M.I. Arshad, H. Anwar, Study of the role of dysprosium substitution in tuning structural, optical, electrical, dielectric, ferroelectric, and magnetic properties of bismuth ferrite multiferroic, Journal of Alloys and Compounds (2022) 165743.

[23] K.C. Patil, S. Aruna, T. Mimani, Combustion synthesis: an update, Current opinion in solid state and materials science 6(6) (2002) 507-512.

[24] K. Cui, M. Sun, J. Zhang, J. Xu, Z. Zhai, T. Gong, L. Hou, C. Yuan, Facile solid-state synthesis of tetragonal $CuFe_2O_4$ spinels with improved infrared radiation performance, Ceramics International 48(8) (2022) 10555-10561.

[25] G. Vinod, K. Rajashekhar, Y. Sandeep, J.L. Naik, Influence of RE-Gd^{3+} ion substitution on structure, morphology, optical, and magnetic analysis of Cu-Cd based nano ferrites synthesized by low-temperature citrate sol-gel auto combustion method, Journal of Magnetism and Magnetic Materials (2022) 169772.

[26] A. Aslam, A. Razzaq, S. Naz, N. Amin, M.I. Arshad, M.A.U. Nabi, A. Nawaz, K. Mahmood, A. Bibi, F. Iqbal, Impact of Lanthanum-Doping on the Physical and Electrical Properties of Cobalt Ferrites, Journal of Superconductivity and Novel Magnetism (2021) 1-10.

[27] M.M. Roni, K. Hoque, T.C. Paul, M. Khan, M.E. Hossain, Synthesis of La-doped $Mn_{0.6}Zn_{0.4}La_xFe_{2-x}O_4$ and the study of its structural, electrical and magnetic properties for high frequency applications, Results in Materials 11 (2021) 100215.

[28] A. Aslam, A.U. Rehman, N. Amin, M. Amami, M. Nabi, H. Alrobei, M. Asghar, N. Morley, M. Akhtar, M.I. Arshad, Sol–Gel Auto-combustion Preparation of $M^{2+} = Mg^{2+}$, Mn^{2+}, Cd^{2+} Substituted $M_{0.25}Ni_{0.15}Cu_{0.25}Co_{0.35}Fe_2O_4$ Ferrites and Their Characterizations, Journal of Superconductivity and Novel Magnetism (2021) 1-11.

[29] N. Amin, A. Razaq, A.U. Rehman, K. Hussain, M.A.U. Nabi, N. Morley, M. Amami, A. Bibi, M.I. Arshad, K. Mahmood, Transport Properties of Ce-Doped Cd Ferrites $CdFe_{2-x}Ce_xO_4$, Journal of Superconductivity and Novel Magnetism 34 (2021) 2945-2955.

[30] M.A. Maksoud, A. El-Ghandour, A. Ashour, M. Atta, S. Abdelhaleem, A.H. El-Hanbaly, R.A. Fahim, S.M. Kassem, M. Shalaby, A. Awed, La^{3+} doped $LiCo_{0.25}Zn_{0.25}Fe_2O_4$ spinel ferrite nanocrystals: Insights on structural, optical and magnetic properties, Journal of Rare Earths 39(1) (2021) 75-82.

[31] N. Amin, M.S.U. Hasan, Z. Majeed, Z. Latif, M.A. un Nabi, K. Mahmood, A. Ali, K. Mehmood, M. Fatima, M. Akhtar, Structural, electrical, optical and dielectric properties of yttrium substituted cadmium ferrites prepared by Co-Precipitation method, Ceramics International 46(13) (2020) 20798-20809.

[32] A. Rajeshwari, I.K. Punithavthy, S.J. Jeyakumar, N. Lenin, B. Vigneshwaran, Dependance of lanthanum ions on structural, magnetic and electrical of manganese based spinel nanoferrites, Ceramics International 46(5) (2020) 6860-6870.

[33] W. Zhang, A. Sun, X. Zhao, N. Suo, L. Yu, Z. Zuo, Structural and magnetic properties of La^{3+} ion doped Ni–Cu–Co nano ferrites prepared by sol–gel auto-combustion method, Journal of Sol-Gel Science and Technology 90 (2019) 599-610.

[34] Y. Dasan, B. Guan, M. Zahari, L. Chuan, Influence of La^{3+} substitution on structure, morphology and magnetic properties of nanocrystalline Ni-Zn ferrite, PloS one 12(1) (2017) e0170075.

[35] M.I.U. Haq, A.u. Rehman, M. Asghar, M.A.U. Nabi, N. Amin, S. Tahir, M.I. Arshad, Influence of Ce^{3+} and La^{3+} substitution on structural & optical parameters and electrical behavior on Mg-Zn ferrites synthesized via co-precipitation method, Journal of Superconductivity and Novel Magnetism 35(3) (2022) 719-732.

[36] J. Massoudi, M. Smari, K. Nouri, E. Dhahri, K. Khirouni, S. Bertaina, L. Bessais, Magnetic and spectroscopic properties of Ni–Zn–Al ferrite spinel: from the nanoscale to microscale, RSC advances 10(57) (2020) 34556-34580.

[37] R. Rani, K.M. Batoo, P. Sharma, G. Anand, G. Kumar, S. Bhardwaj, M. Singh, Structural, morphological and temperature dependent electrical traits of $Co_{0.9}Zn_{0.1}In_xFe_{2-x}O_4$ spinel nano-ferrites, Ceramics International 47(21) (2021) 30902-30910.

[38] V. Chaudhari, R. Kadam, M. Mane, S.E. Shirsath, A. Kadam, D. Mane, Effect of La^{3+} impurity on magnetic and electrical properties of Co–Cu–Cr–Fe nanoparticles, Journal of Nanoscience and Nanotechnology 15(6) (2015) 4268-4275.

[39] M. Akram, S. Akhlaq, M.I. Arshad, N. Amin, A.A. Ifseisi, M. Akhtar, N.T.K. Thanh, N. Morley, S. Sadiq, S. Hussain, Improving the structural and transport properties of cadmium ferrites with the addition of cerium for high frequency applications, Solid State Communications 373 (2023) 115317.

[40] G. Abbas, A.U. Rehman, W. Gull, M. Afzaal, N. Amin, L. Ben Farhat, M. Amami, N.A. Morley, M. Akhtar, M.I. Arshad, Impact of Co^{2+} on the spectral, optoelectrical, and dielectric properties of $Mg_{0.25}Ni_{0.25}Cu_{0.5-x}Co_xFe_{1.97}La_{0.03}O_4$ ferrites prepared via sol–gel auto-combustion route, Journal of Sol-Gel Science and Technology 101(2) (2022) 428-442.

[41] X. Zhu, Z. Yu, X. Yu, S. Jin, X. Liu, X. Gu, Optimization of room-temperature temperature coefficient of resistivity of $La_{0.75-x}K_{0.19+x}Sr_{0.06}MnO_3$ ($0.00 \leq x \leq 0.06$) ceramics by La and K content adjustment, Ceramics International 49(5) (2023) 7640-7648.

[42] A.U. Rehman, N. Amin, M.B. Tahir, M.A. un Nabi, N. Morley, M. Alzaid, M. Amami, M. Akhtar, M.I. Arshad, Evaluation of spectral, optoelectrical, dielectric, magnetic, and morphological properties of RE^{3+} (La^{3+}, and Ce^{3+}) and Co^{2+} co-doped $Zn_{0.75}Cu_{0.25}Fe_2O_4$ ferrites, Materials Chemistry and Physics 275 (2022) 125301.

[43] A.U. Rehman, S. Sharif, H. Hegazy, N. Morley, N. Amin, M. Akhtar, M.I. Arshad, Z. Farooq, Z. Munir, T. Munir, Low dielectric loss, and enhanced magneto-dielectric properties of $Cu_{0.5}Cd_{0.5-x}Co_xFe_2O_4$ ferrites via Co^{2+} substitution, Materials Today Communications (2023) 105371.

[44] A.S. Priya, D. Geetha, J. Madhavan, Synthesis and Structural, Dielectric and Photocatalytic Properties of (Ti, La)-co-Doped Calcium Ferrite Ceramic Powders, Arabian Journal for Science and Engineering (2022) 1-11.

[45] B. Philippa, M. Stolterfoht, P.L. Burn, G. Juška, P. Meredith, R.D. White, A. Pivrikas, The impact of hot charge carrier mobility on photocurrent losses in polymer-based solar cells, Scientific reports 4(1) (2014) 1-7.

[46] M. Abdullah-Al-Mamun, M. Sarker, M. Hasan, M. Haque, F. Khan, M. Rahman, M. Khan, Effect of Er substitution on the magnetic, Mössbauer spectroscopy and dielectric properties of $CoFe_{2-x}Er_xO_4$ (x= 0.00, 0.01, 0.03, 0.05) nanoparticles, Results in Physics 29 (2021) 104698.

[47] M. Naagar, S. Chalia, S. Kharbanda, P. Thakur, A. Thakur, Correlating tailored saturation magnetization of normal-inverse spinels with noncollinear magnetic ordering, Journal of Materials Science: Materials in Electronics 34(6) (2023) 473.

[48] M.K. Bharti, S. Chalia, P. Thakur, A. Thakur, Effect of lanthanum doping on microstructural, dielectric and magnetic properties of $Mn_{0.4}Zn_{0.6}Cd_{0.2}La_xFe_{1.8-x}O_4$ (0.0≤ x≤ 0.4), Journal of Superconductivity and Novel Magnetism 34(10) (2021) 2591-2600.

[49] X. Zhou, Y. Zhou, L. Zhou, J. Wei, J. Wu, D. Yao, Effect of Gd and La doping on the structure, optical and magnetic properties of NiZnCo ferrites, Ceramics International 45(5) (2019) 6236-6242.

[50] P. Palaniappan, N. Lenin, R. Uvarani, Structural characteristics and electrical properties of lanthanum-doped nanoferrites synthesized by sonochemical method, Applied Physics A 128(9) (2022) 814.

[51] S.K. Gore, U.B. Tumberphale, S.S. Jadhav, S.F. Shaikh, A.M. Al-Enizi, A.u.H.S. Rana, R.N. Khule, S.D. Raut, T.S. Gore, R.S. Mane, Grain and grain boundaries influenced magnetic and dielectric properties of lanthanum-doped copper cadmium ferrites, Journal of Materials Science: Materials in Electronics 33(10) (2022) 7636-7647.

[52] K. Praveena, K. Sadhana, Ferromagnetic properties of Zn substituted spinel ferrites for high frequency applications, International Journal of Scientific and Research Publications 5(4) (2015) 1-21.

[53] Z. Latifa, A. Rehmana, M. Yusufb, N. Amina, M. Arshada, Estimation of the spectral, electrical, and dielectric properties of Mn-Cu-Cd-Gd ferrite\graphene nanoplatelets composites, Journal of Ovonic Research 18(4) (2022) 627-635.

[54] A. Aslam, A.U. Rehman, N. Amin, M. Amman, M. Akhtar, N. Morley, M.S. Al-Sharif, M. Hessien, K.A. El-Nagdy, M.I. Arshad, To study the structural, electrical, and magnetic properties of M (M= Mg^{2+}, Mn^{2+}, and Cd^{2+}) doped Cu-Ni-Co-La spinel ferrites, Materials Chemistry and Physics 294 (2023) 127034.

[55] K. Mehmood, A.U. Rehman, N. Amin, N. Morley, M.I. Arshad, Graphene nanoplatelets/Ni-Co-Nd spinel ferrite composites with improving dielectric properties, Journal of Alloys and Compounds 930 (2023) 167335.

[56] M.I. Arshad, M. Hasan, A.U. Rehman, M. Akhtar, N. Amin, K. Mahmood, A. Ali, T. Trakoolwilaiwan, N.T.K. Thanh, Structural, optical, electrical, dielectric, molecular vibrational and magnetic properties of La^{3+} doped Mg–Cd–Cu ferrites prepared by Co-precipitation technique, Ceramics International 48(10) (2022) 14246-14260.

[57] A.U. Rehman, G. Abbas, B. Ayoub, N. Amin, M.A. un Nabi, N.A. Morley, M. Akhtar, M.I. Arshad, M.U. Khalid, M. Afzaal, Impact of Ni^{2+} on the structural, optical, electrical, and dielectric properties of $Cu_{0.25}Co_{0.25}Mg_{0.5-x}Ni_xCe_{0.03}Fe_{1.97}O_4$ spinel ferrites synthesized via sol-gel auto combustion (SGAC) route, Materials Science and Engineering: B 291 (2023) 116407.

Table 1: Structural parameters for La-CLCF samples

x	D (nm)	d (Å)	a (Å)	δ (nm^{-2})	V (Å)^3	H_A (Å)	H_B (Å)	γ_p (Å)	d_X (g/cm^3)	ρ_B (g/cm^3)	ρ_R (%)	P (%)	d_X (g/cm^3)
0.00	13.94	2.496	8.281	0.0051	567.88	3.585	2.927	0.741	5.140	3.01	170.78	41.44	5.140
0.01	15.56	2.500	8.292	0.0041	570.18	3.590	2.931	0.743	5.139	3.16	162.63	38.51	5.139
0.02	14.13	2.508	8.319	0.0050	575.75	3.602	2.940	0.745	5.108	3.39	150.70	33.64	5.108
0.03	11.26	2.515	8.341	0.0078	580.45	3.611	2.948	0.747	5.086	3.58	142.08	29.61	5.086
0.04	10.91	2.518	8.353	0.0083	582.82	3.616	2.952	0.748	5.084	3.85	132.07	24.28	5.084
0.05	10.49	2.529	8.389	0.0091	590.50	3.632	2.965	0.751	5.037	3.96	127.21	21.38	5.037

Table 2 Electrical parameters of La-CLCF samples

x	$\rho \times 10^9$ at 303 K (Ω cm)	$\eta \times 10^{22}$	$\mu_d \times 10^{-21}$ at 303 K (cm^2 V^{-1}s^{-1})	ΔE (eV)	T_C (K)
0.00	0.008	1.732	14.8835	0.307	353
0.01	0.122	1.803	0.9491	0.408	363
0.02	0.295	1.918	0.3678	0.451	373
0.03	1.523	2.008	0.0681	0.531	383
0.04	13.167	2.141	0.0074	0.715	393
0.05	14.275	2.184	0.0068	0.786	403

Table 3: Magnetic properties of La-CLCF samples

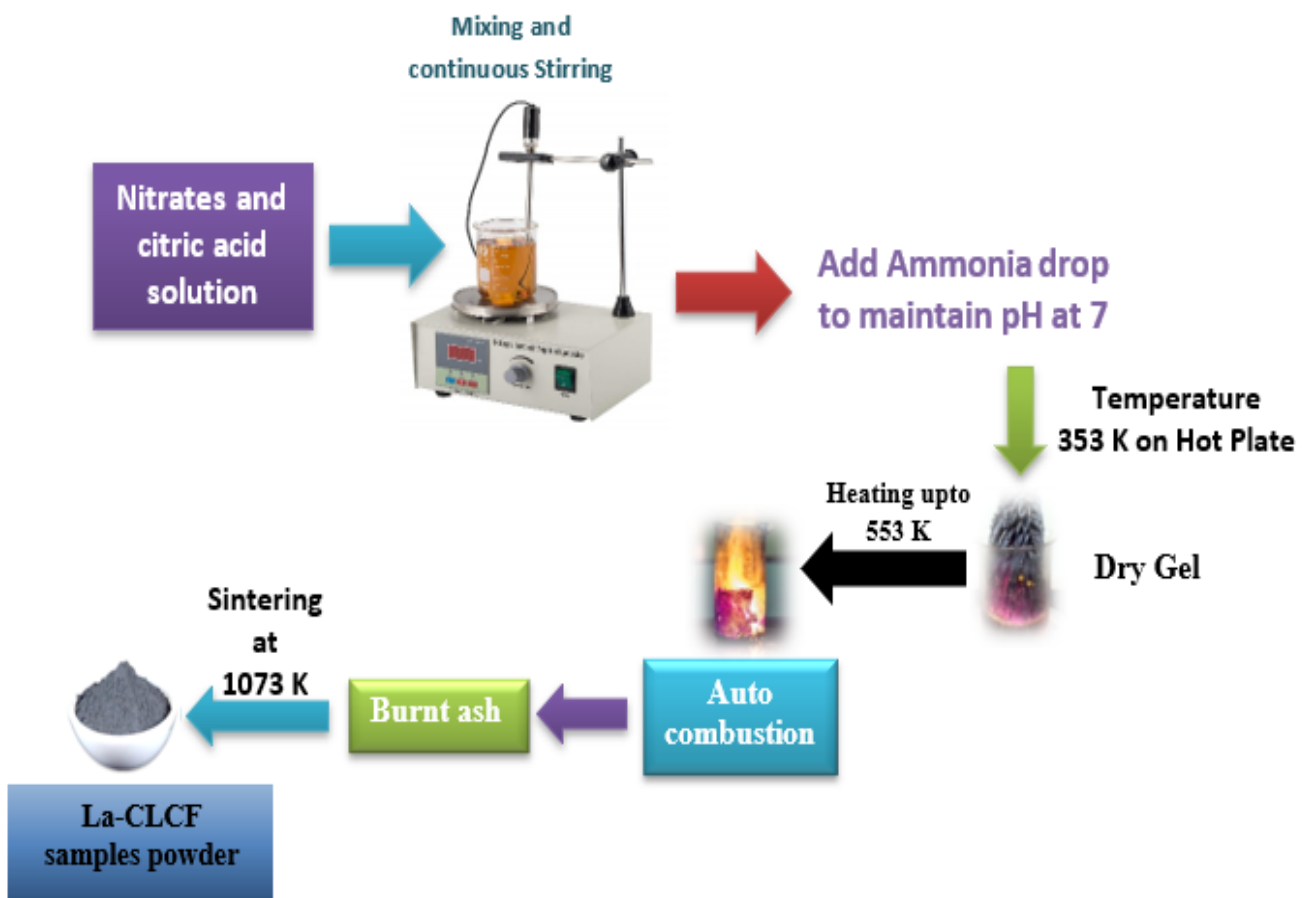| x	M_s (emu/g)	M_r (emu/g)	H_C (Oe)	S_q ratio	K (erg/cm^3)	ω_m (GHz)
0.00	92.23	24.4	189.47	0.264	18202.93	20.39
0.01	117.33	37.11	359.53	0.316	43941.30	25.93
0.02	95.71	32.02	430.88	0.334	42957.83	21.15
0.03	87.91	21.78	242.95	0.247	22247.64	19.43
0.04	85.81	23.41	346.33	0.272	30956.85	18.97
0.05	83.22	28.83	391.61	0.346	33947.69	18.39

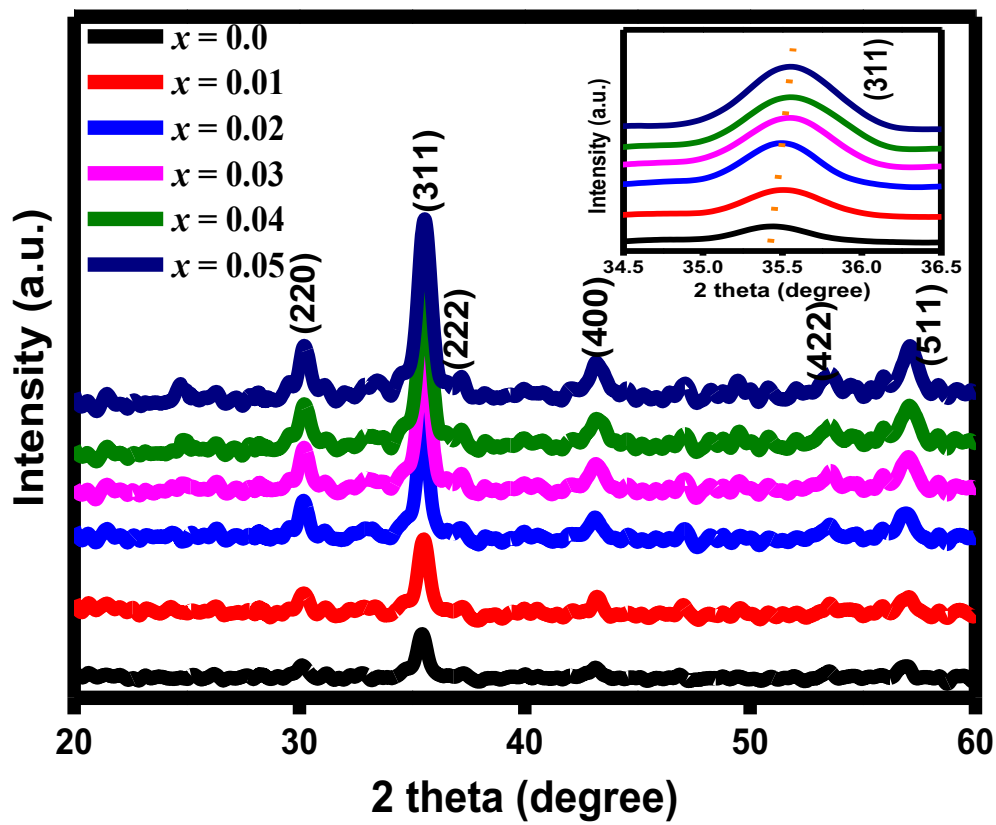**Fig. 1** SGAC process for the synthesis of La-CLCF samples
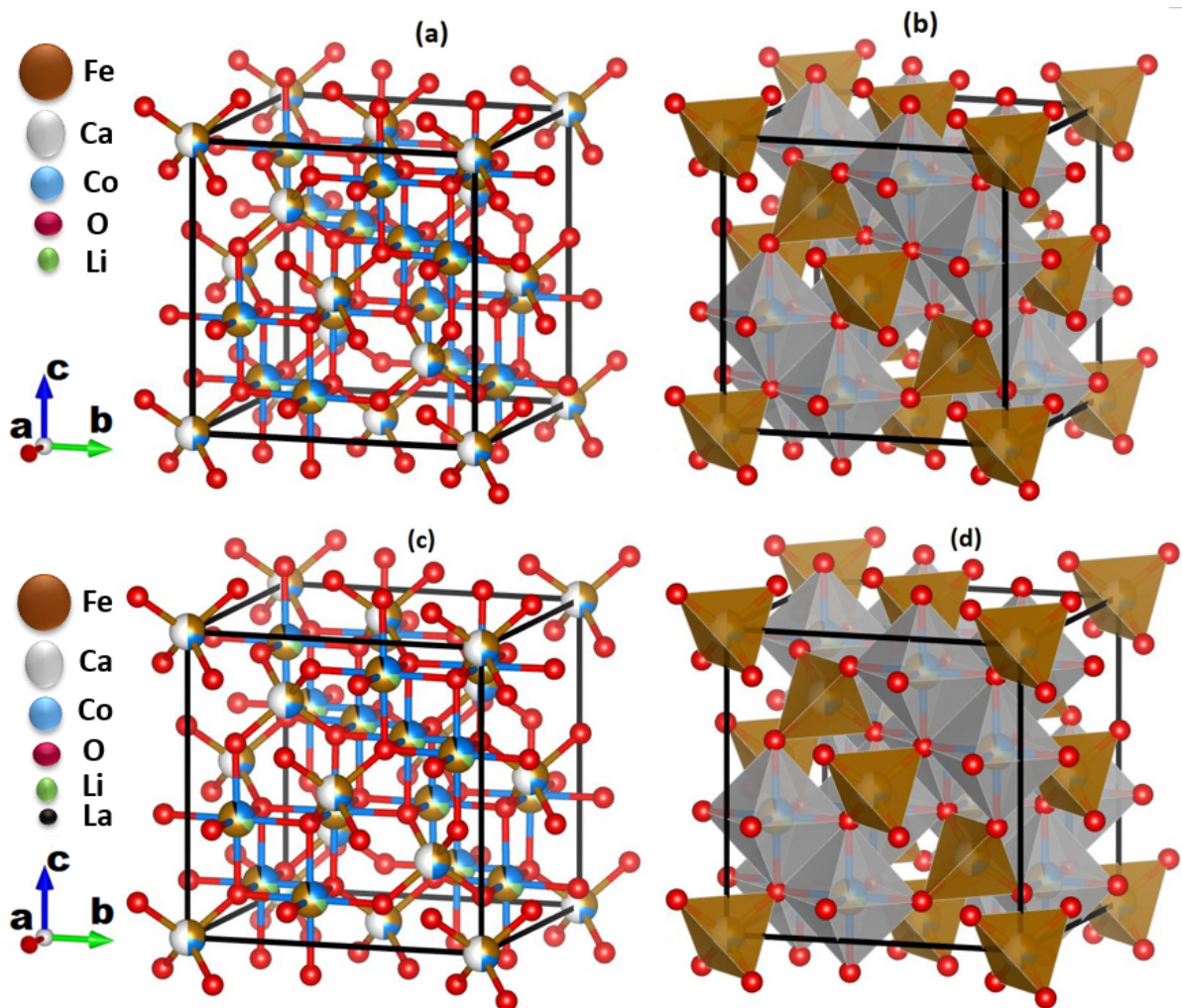
Fig. 2 XRD spectra for La-CLCF samples

Fig. 3(a) Unit cell structure for CLCF sample **(b)** tetrahedral and octahedral sites in the unit cell structure of CLCF sample **(c)** unit cell structure for sample $x = 0.01$ **(d)** tetrahedral and octahedral sites in unit cell structure for sample $x = 0.01$
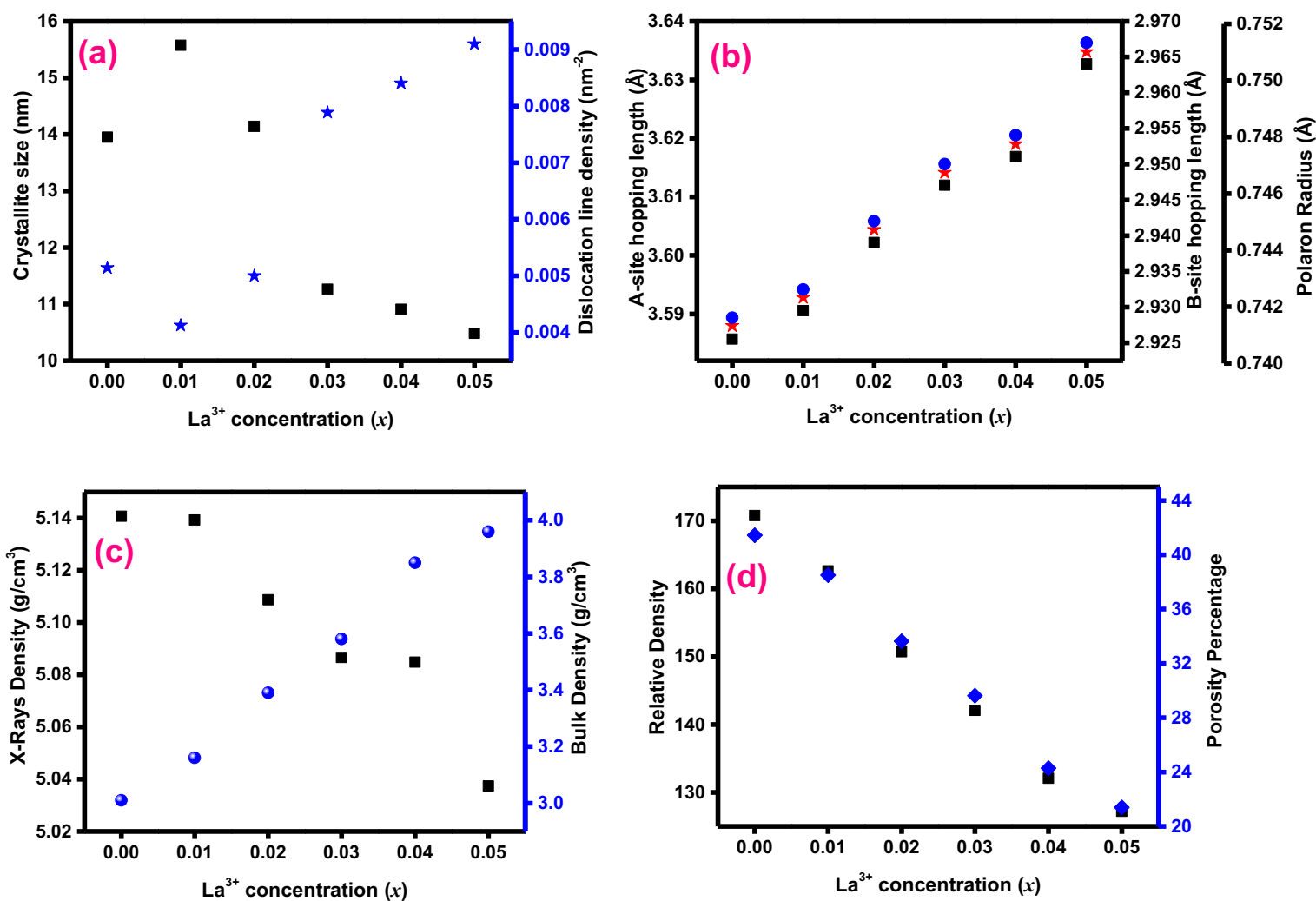
Fig. 4 La^{3+} concentration (x) *versus* **(a)** crystallite size and dislocation line density **(b)** *A*- and *B*- sites hopping length with polaron radius **(c)** X-ray and bulk densities **(d)** relative density and porosity for all the samples
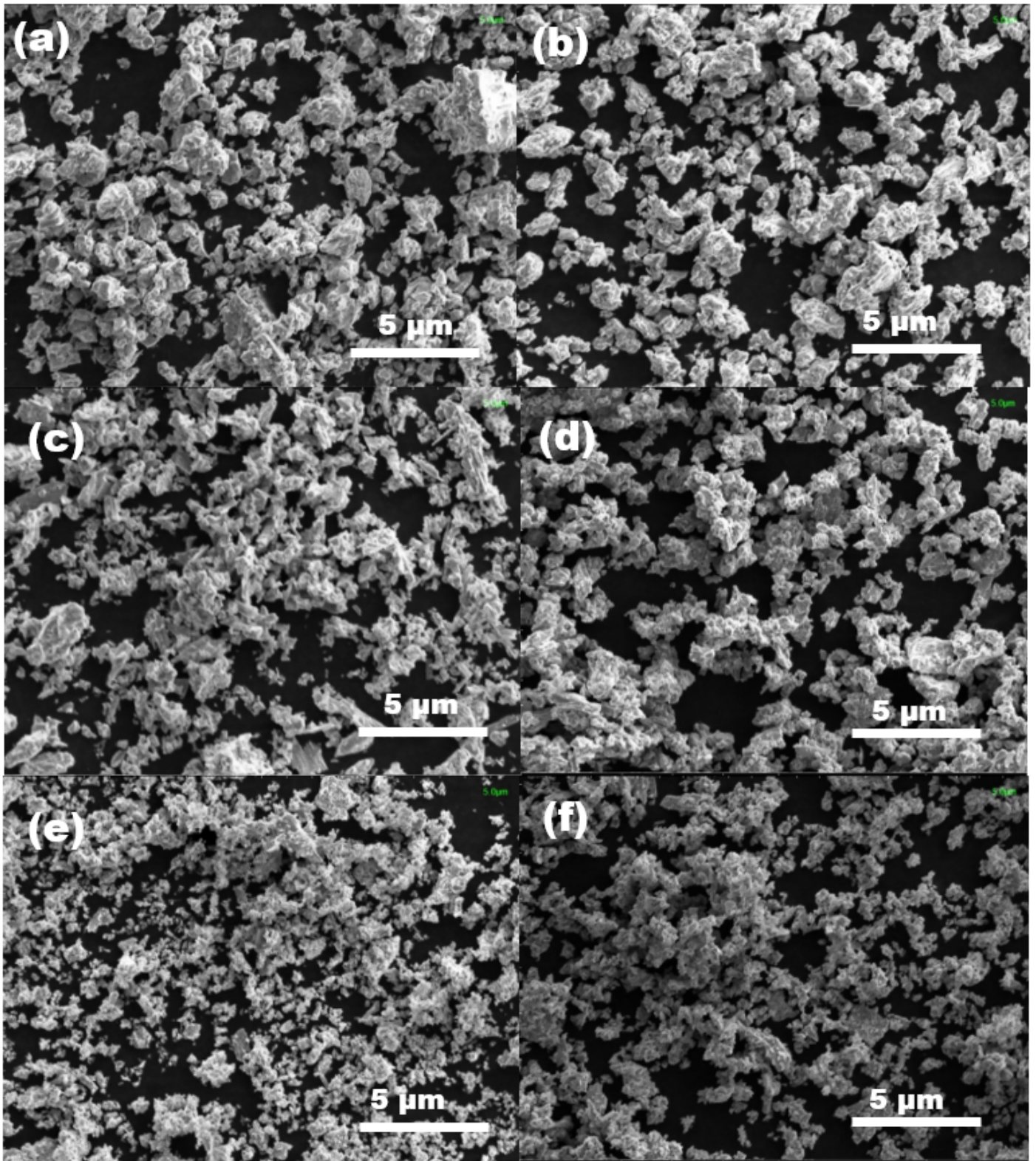
Fig. 5 SEM micrographs **(a)** for sample $x = 0.0$ **(b)** for sample $x = 0.01$ **(c)** for sample $x = 0.02$ **(d)** for sample $x = 0.03$ **(e)** for sample $x = 0.04$ **(f)** for sample $x = 0.05$ at 5 μm scale
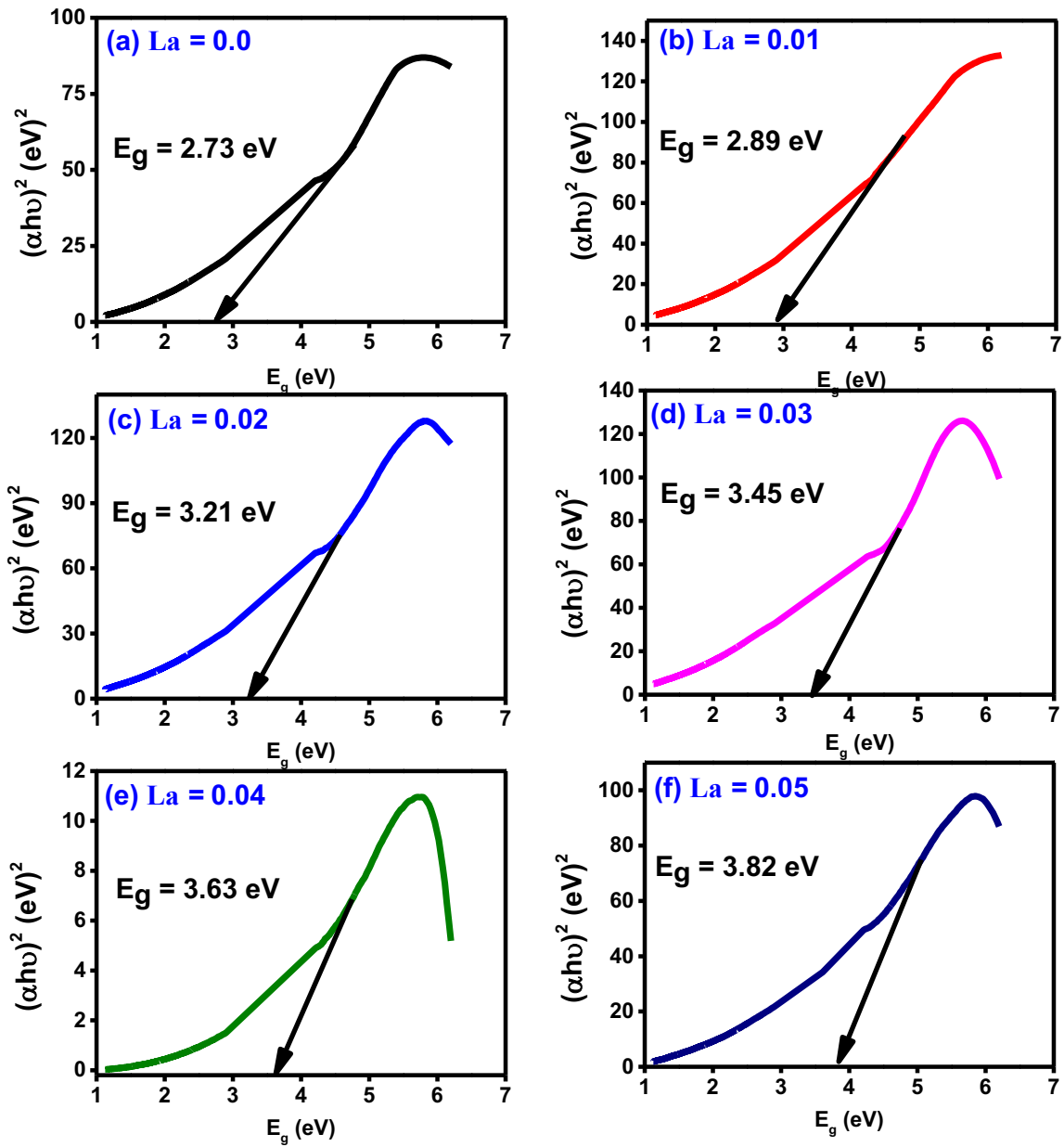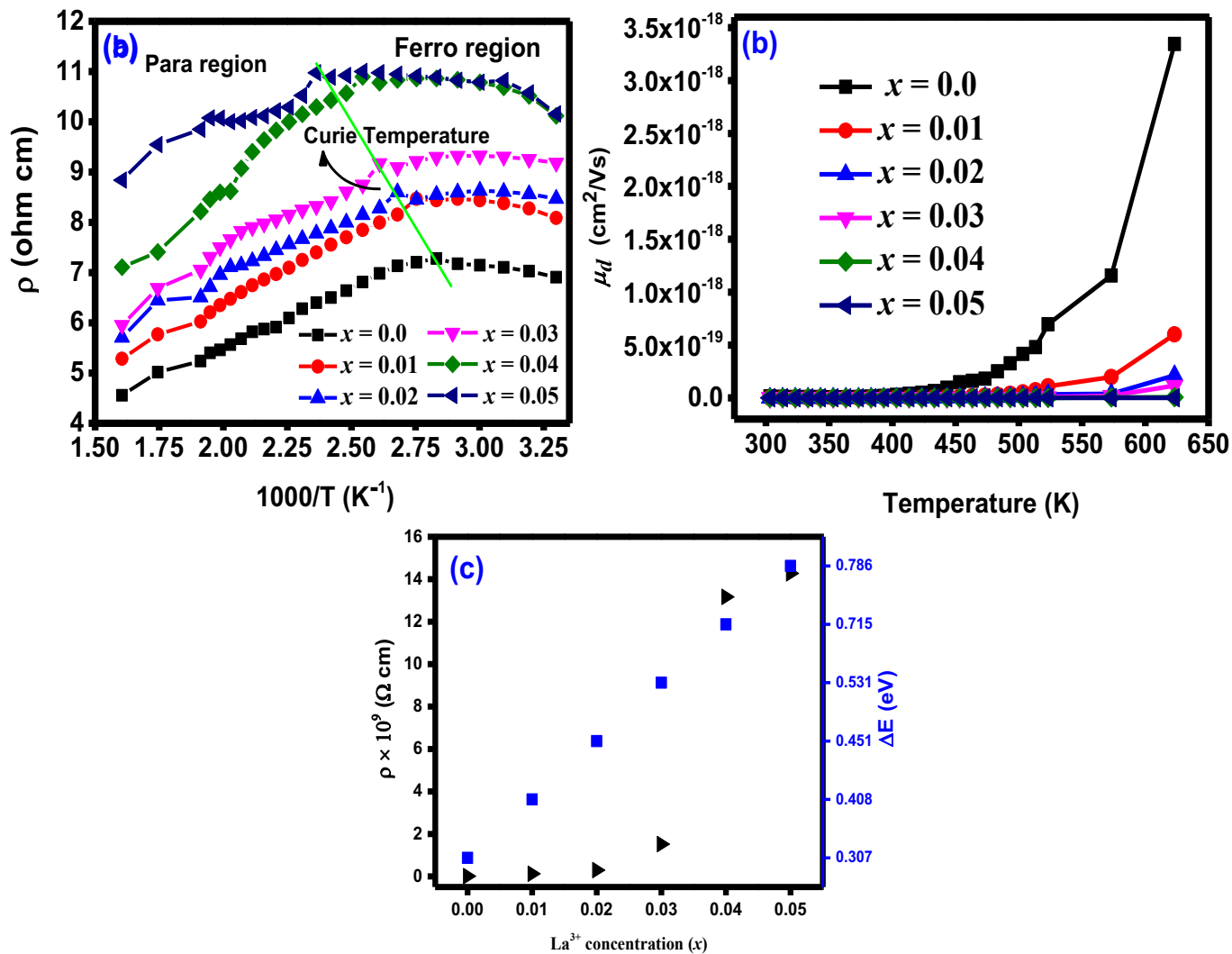
Fig. 6 Tauc plots **(a)** for sample $x = 0.0$ **(b)** for sample $x = 0.01$ **(c)** for sample $x = 0.02$ **(d)** for sample $x = 0.03$ **(e)** for sample $x = 0.04$ **(f)** for sample $x = 0.05$

Fig. 7(a) Arrhenius plots **(b)** drift mobility *versus* temperature for La-CLCF samples **(c)** resistivity at 303 K, and activation energy *versus* La^{3+} concentration
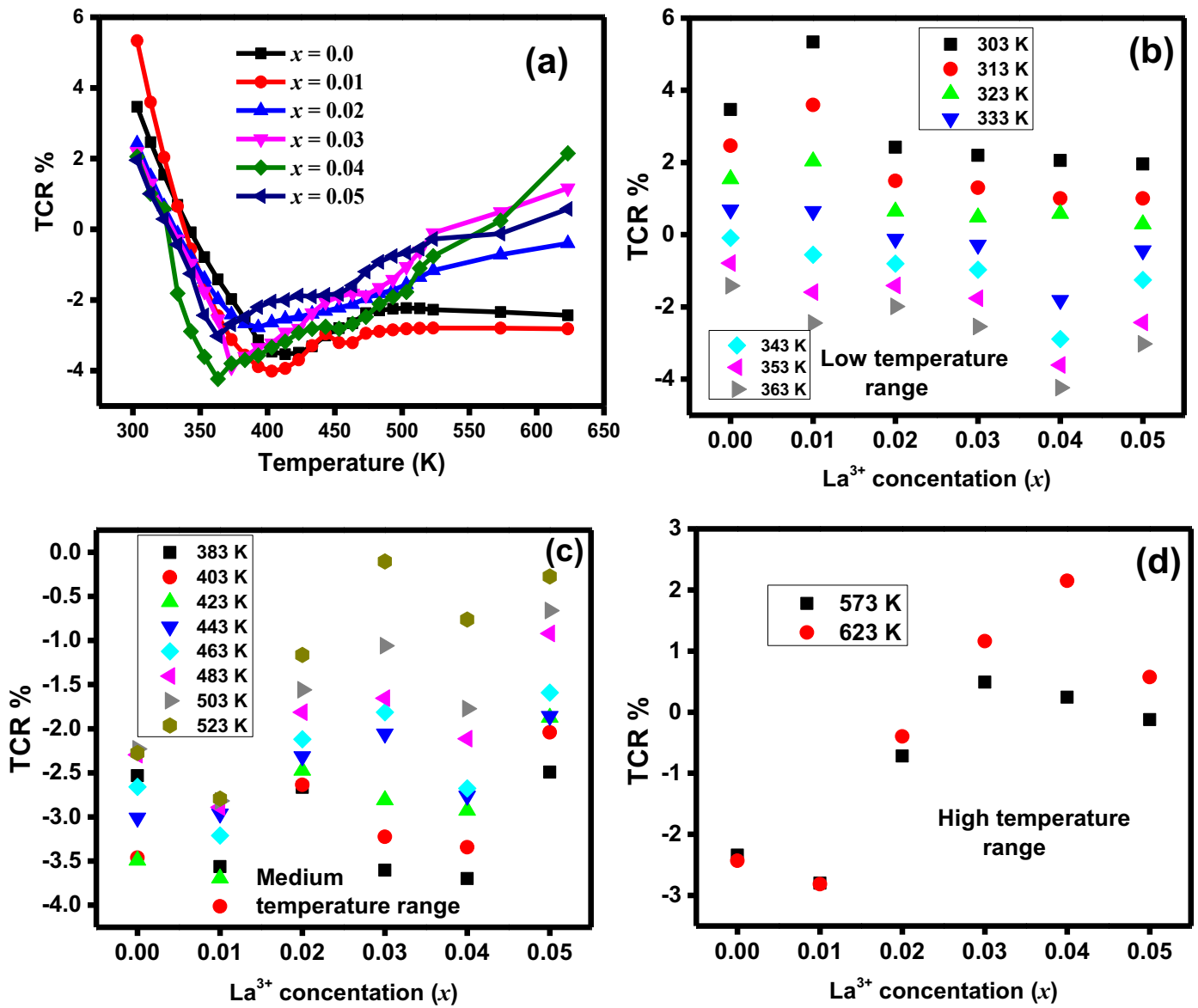
Fig. 8(a) Temperature coefficient of resistance *versus* temperature plots **(b)** Temperature coefficient of resistance *versus* La³⁺ concentration (*x*) at temperature 303 K to 363 K **(c)** Temperature coefficient of resistance *versus* La³⁺ concentration (*x*) at temperature 383 K to 523 K **(d)** temperature coefficient of resistance *versus* La³⁺ concentration (*x*) at temperature 373 K to 623 K
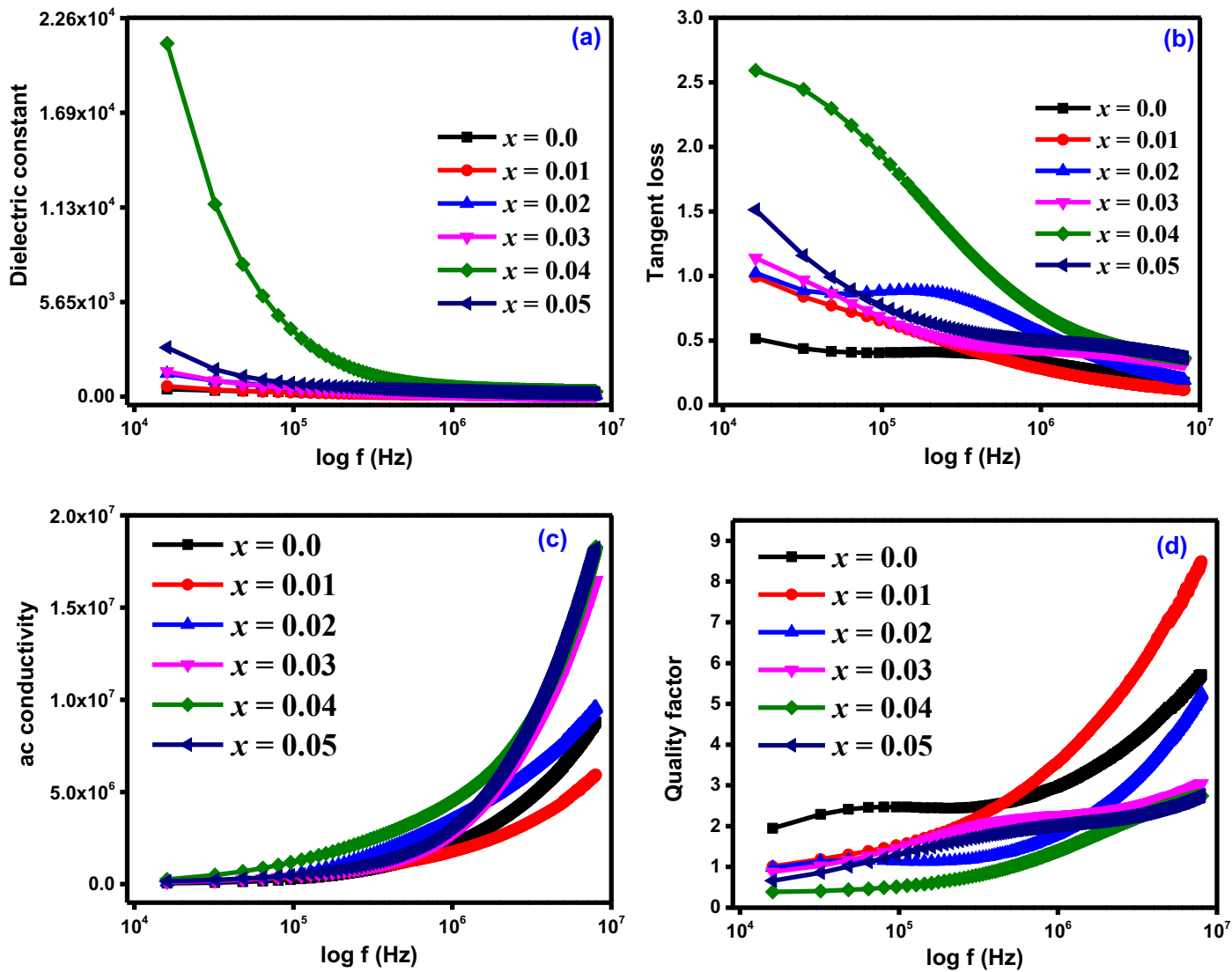
Fig. 9(a) Dielectric constant *versus* the log of frequency for La-CLCF samples **(b)** Tangent loss *versus* the log of frequency for La-CLCF samples **(c)** *ac* conductivity *versus* the log of frequency for La-CLCF samples **(c)** Quality factor *versus* the log of frequency for La-CLCF samples
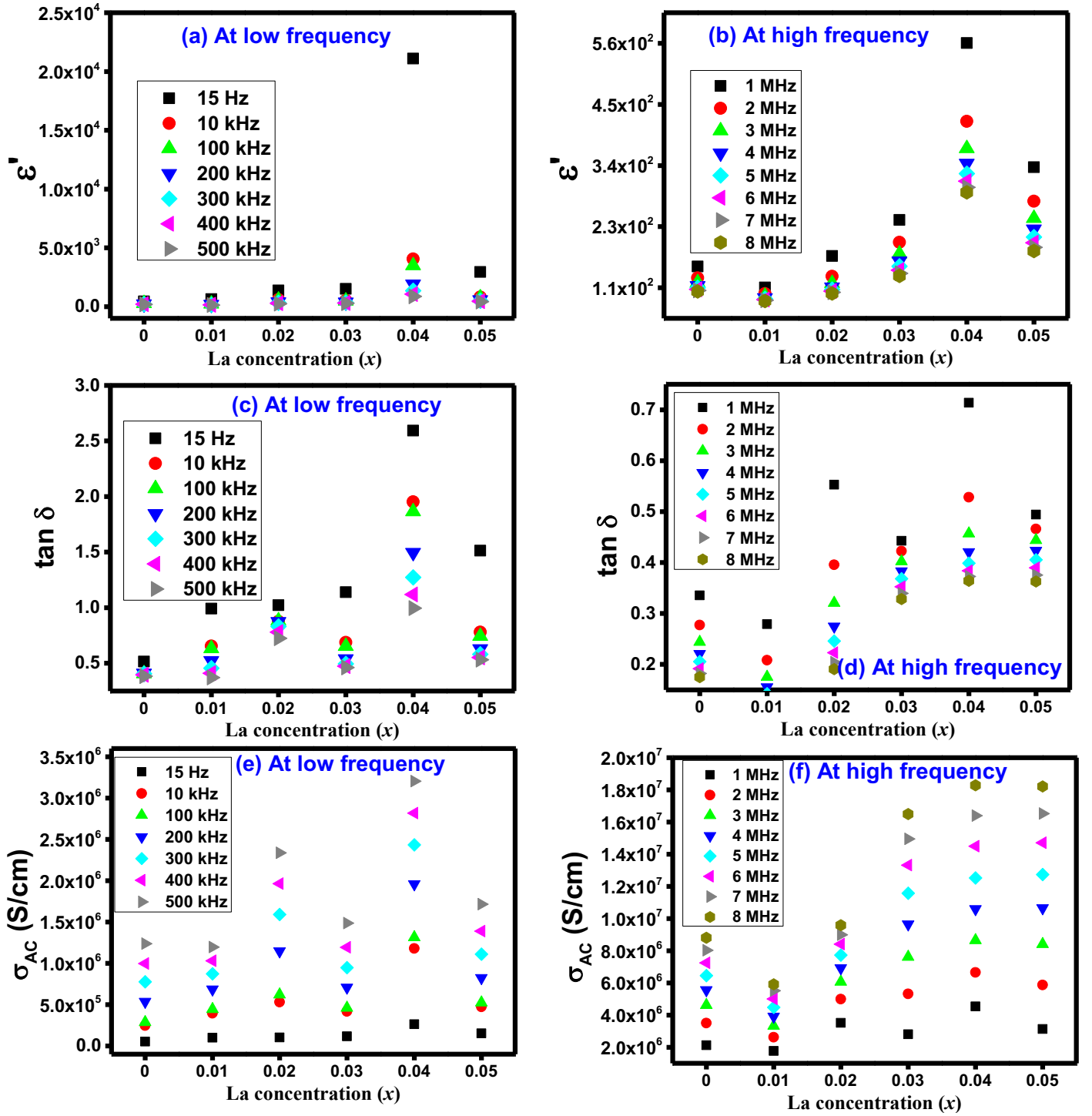
23

Fig. 10(a) dielectric constant *versus* La^{3+} concentration (x) at low-frequency range **(b)** dielectric constant *versus* La^{3+} concentration (x) at high-frequency range **(c)** tangent loss *versus* La^{3+} concentration (x) at low-frequency range **(d)** tangent loss *versus* La^{3+} concentration (x) at high-frequency range **(e)** *ac* conductivity *versus* La^{3+} concentration (x) at low-frequency range **(f)** *ac* conductivity *versus* La^{3+} concentration (x) at high-frequency range
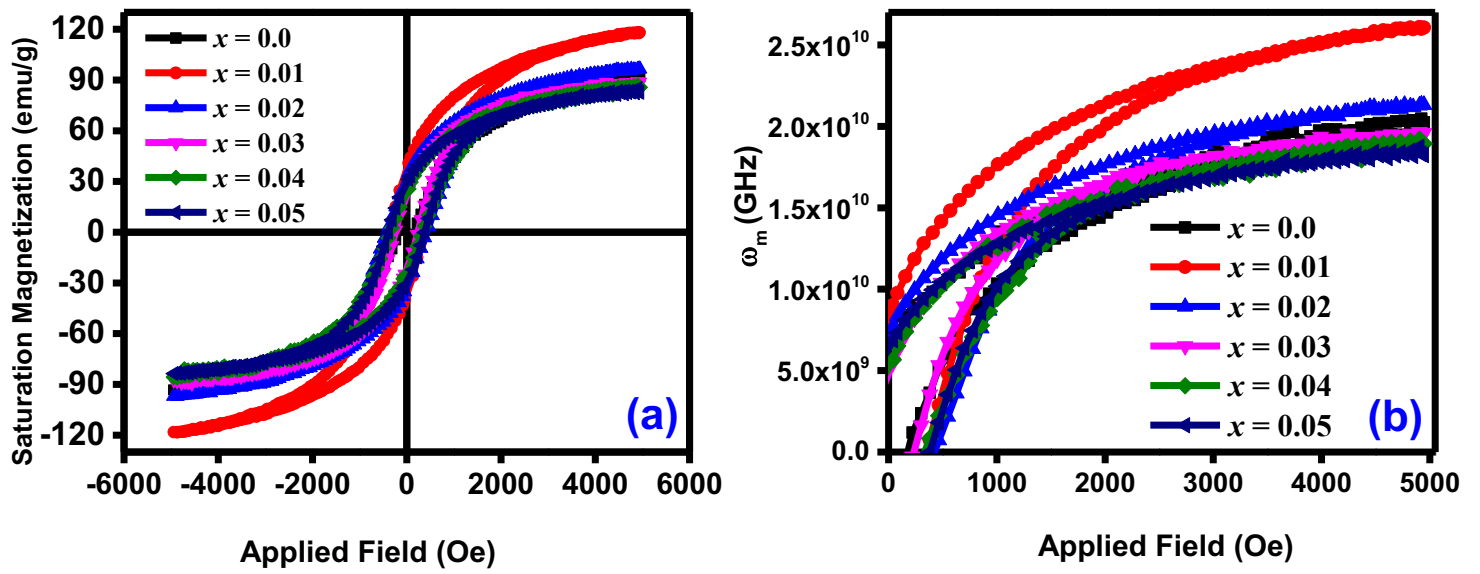
24

Fig. 11(a) Hysteresis loops for La-CLCF samples (b) applied field *versus* microwave operating frequency for La-CLCF samples